nature photonics

Article https://doi.org/10.1038/s41566-025-01832-9

A high-speed heterogeneous lithium tantalate silicon photonics platform

Received: 13 February 2025

Accepted: 6 December 2025

Published online: 13 January 2026

Check for updates

A list of authors and their affiliations appears at the end of the paper

The rapid expansion of cloud computing and artificial intelligence has driven the demand for faster optical components in data centres to unprecedented levels. A key advancement in this field is the integration of multiple photonic components onto a single chip, enhancing the performance of optical transceivers. Here silicon photonics, benefiting from mature fabrication processes, has gained prominence in both academic research and industrial applications. The platform combines modulators, switches, photodetectors and low-loss waveguides on a single chip. However, emerging telecommunication standards require modulation speeds that exceed the capabilities of silicon-based modulators. To address these limitations, thin-film lithium niobate has been proposed as an alternative to silicon photonics, offering a low voltage–length product and exceptional high-speed modulation properties. More recently, the first demonstrations of thin-film lithium tantalate circuits have emerged, potentially addressing some of the disadvantages of lithium niobate, enabling a reduced bias drift and enhanced resistance to optical damage. As such, this material arises as a promising candidate for next-generation photonic platforms. However, a persistent drawback of such platforms is the lithium contamination, which complicates integration with CMOS fabrication processes. Here we present for the first time the integration of lithium tantalate onto a silicon photonics chip. This integration is achieved without modifying the standard silicon photonics process design kit. Our device achieves low half-wave voltage (3.5 V), low insertion loss (2.9 dB) and high-speed operation (>70 GHz), paving the way for next-generation applications. By minimizing lithium tantalate material use, our approach reduces costs while leveraging existing silicon photonics technology advancements, in particular supporting ultra-fast monolithic germanium photodetectors and established process design kits.

The exponential growth in data network traffic leads to hardly sustainable power consumption levels in data centres. Photonic integration, initially developed on indium phosphide[1] and more recently on silicon photonic (SiPho) platforms, has substantially enhanced data rates while minimizing power consumption[2]. Silicon photonic integrated circuits (Si-PICs) enable the dense integration of complex optical functionalities on silicon chips. The technology leverages standard fabrication techniques used in the CMOS electronics industry, allowing for high-volume, high-yield and low-cost production. A typical SiPho platform (Fig. 1) integrates several key components, including Si waveguides with dopants for high-speed modulation, heaters for efficient low-speed thermal tuning, a silicon nitride (SiN) layer for low-loss propagation and high-quality filtering, and germanium photodetectors. The latter have demonstrated bandwidths exceeding 200 GHz (ref. 3). However, emerging standards[4] may require baud rates surpassing 200 GBd, which exceed the performance limits of current Si photonic modulators.

e-mail: Margot.Niels@UGent.be; Tom.Vanackere@UGent.be; Bart.Kuyken@UGent.be; Maximilien.Billet@UGent.be

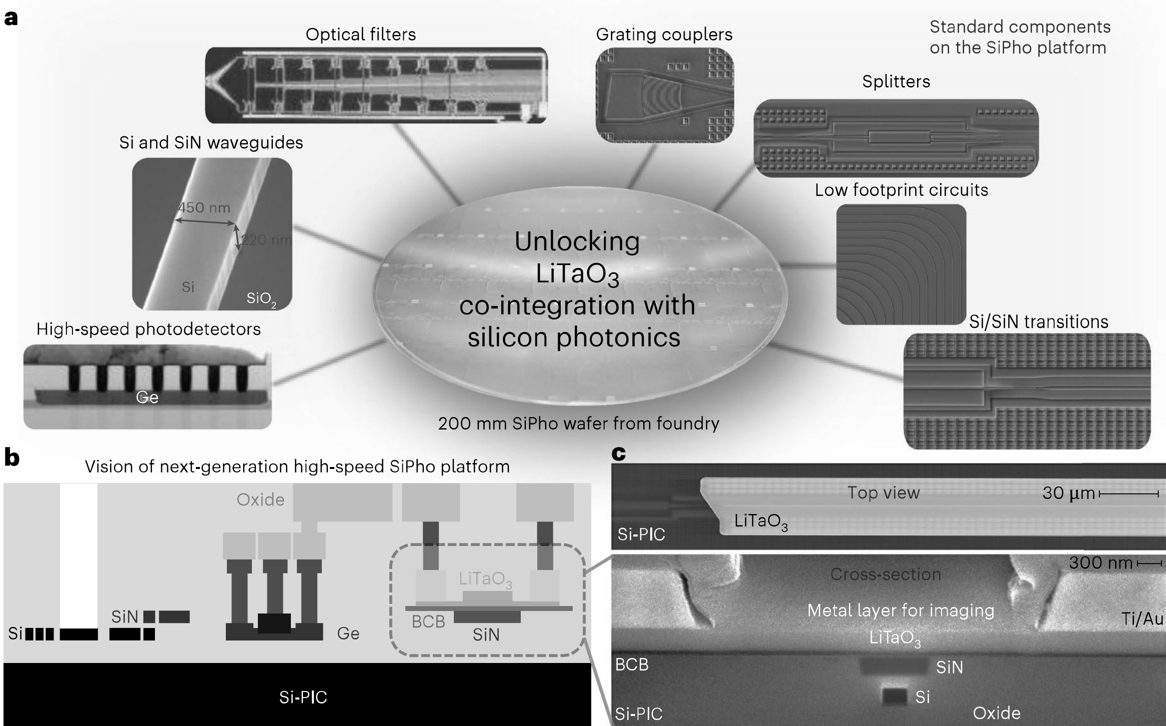

Fig. 1 | Next-generation high-speed SiPho platform. a, Generic view of a state-of-the-art SiPho platform with its basic components. **b**, Cross-section of the vision of a high-speed Si-PIC: next to the components already offered, lithium tantalate ($LiTaO_3$) modulators need to be integrated. **c**, SEM (colourized) picture after the integration of $LiTaO_3$ on a Si-PIC and focused ion beam cross-section (colourized) of a heterogeneous EO device on a Si-PIC.

To overcome this limitation, various alternative platforms are under investigation. Here the heterogeneous integration of novel electro-optic (EO) materials on Si-PICs is gaining substantial attention. Barium titanate (BTO) presents a promising option owing to its capability for direct growth on Si layers and its compatibility with CMOS fabrication processes[5]. While high-speed operation has been achieved, challenges such as high permittivity dispersion and the requirement for a constant bias persist. Alternative approaches include the integration of organic materials[6], plasmonics[7–10], III–V semiconductors[11,12] and graphene[13–16]. However, thin-film lithium niobate (TFLN) has emerged as a standout material, offering a combination of low optical loss and a strong, fast EO Pockels effect[17]. In demonstrations, bandwidths exceeding 100 GHz (ref. 18) have been achieved on monolithic TFLN platforms. Moreover, lithium niobate ($LiNbO_3$) has been heterogeneously integrated onto Si and SiN platforms. Heterogeneous integration allows to combine the mature SiPho platforms and their components (for example, high-speed photodetectors) with a high-speed $LiNbO_3$ modulator.

Very recently, lithium tantalate ($LiTaO_3$) has emerged as an alternative to $LiNbO_3$ (refs. 19–22). The material has a similar EO coefficient as $LiNbO_3$. Yet, it shows a much weaker photorefractive effect and a higher damage threshold. More recently, the first demonstrations of thin-film lithium tantalate circuits have emerged, addressing some of the disadvantages of lithium niobate. For example, in a number of experiments, it seems that $LiTaO_3$ enables a reduced bias drift[20,23,24]. So far, only demonstrations on a monolithic platform have been shown. As with monolithic $LiNbO_3$ optical waveguide platforms, however, the route towards high volume production in CMOS fabs is less clear owing to the contamination caused by lithium[25]. Moreover, the integration of other components, such as high-speed detectors, is not obvious at the moment.

In this work, we present the first demonstration of the heterogeneous integration of $LiTaO_3$ onto a Si-PIC. The integrated modulator is compatible with the Si-PIC's process design kit (PDK), ensuring full compatibility with platform components and enabling their optimal functionality. Leveraging the existing PDK, we achieve seamless integration of EO components without compromising the performance of the established. Using a back-end of line integration approach, based on micro-transfer printing (µTP)[26,27], we ensure compatibility with the entire wafer stack, facilitating co-integration with critical components such as heaters, filters and germanium photodetectors (Extended Data Fig. 4). A conceptual view of the heterogeneous platform is illustrated in Fig. 1. Heterogeneous integration techniques such as die-to-wafer and wafer-to-wafer bonding[28–31] as well as µTP[32–34] have been successfully used for the heterogeneous integration of $LiNbO_3$ onto SiPho platforms. Although die and wafer bonding are more established techniques in industry, the latter is limited by the size of the current widely available 150 mm TFLN wafers. However, the recent availability of larger 200 mm $LiNbO_3$ wafers enables now the full coverage of 200 mm SiPho wafers. A key advantage of both the die-to-wafer and wafer-to-wafer bonded $LiNbO_3$ films lies in its relaxed alignment tolerances, as device positioning is defined by lithographic techniques. In this work, µTP was used for the heterogeneous integration of the $LiTaO_3$ membranes. This technique offers, for example, for $LiNbO_3$, a versatile approach for back-end of line integration of pre-fabricated (poled) $LiNbO_3$ devices onto SiPho platforms[33,35], while minimizing post-processing complexity and contamination risks. µTP further enables three-dimensional integration into deep recesses, supports low-temperature post-processing and allows integration on wafers of any size. In addition, it facilitates multi-material integration, broadening the scope of heterogeneous device architectures[27].

The unbalanced Mach–Zehnder modulator (MZM), presented as a demonstrator in this work, achieves a measured bandwidth exceeding 70 GHz (limited by measurement equipment) and is estimated to reach 90 GHz. It also exhibits a voltage–length product of 2.3 V cm, comparable to recent results from monolithic $LiTaO_3$ platforms[21]. Furthermore, the hybrid phase modulator in the arms of the Mach–Zehnder has a total insertion loss of 2.9 dB, dominated by metal losses caused by a fabrication misalignment (1.6 dB). Finally, data modulation up to

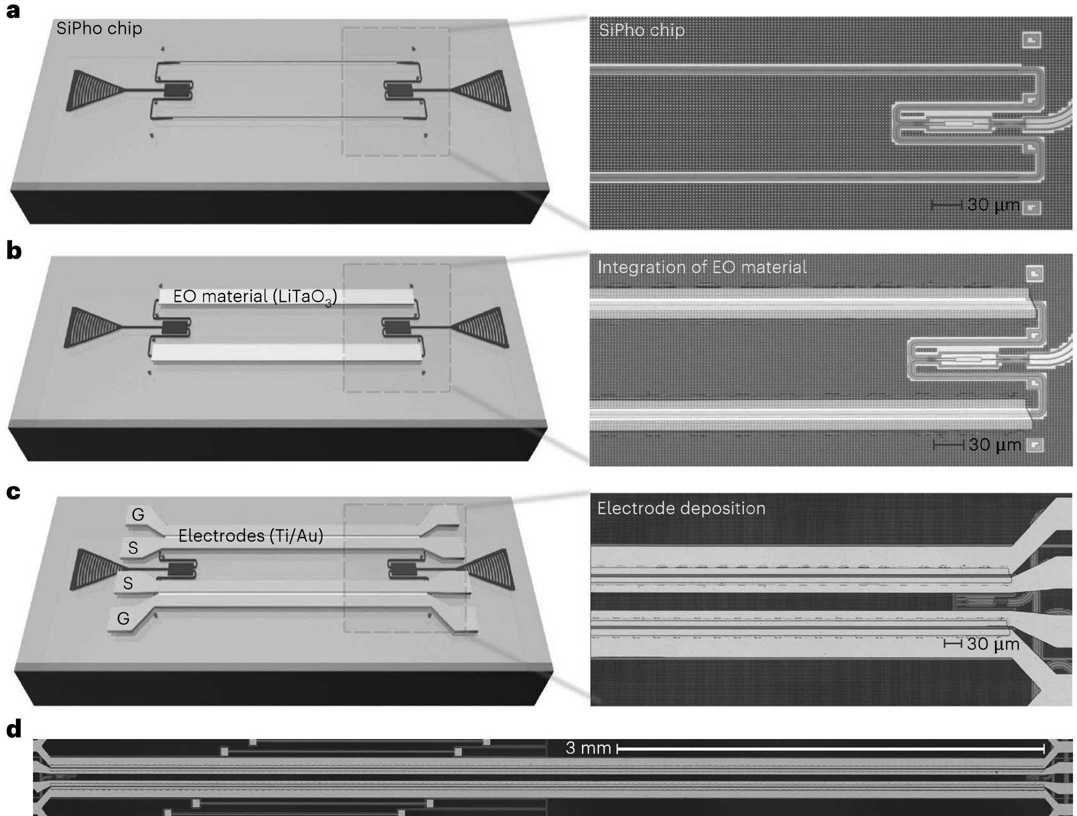

Fig. 2 | Integration flow of $LiTaO_3$ on a SiPho chip. a, Architecture of the passive Si and SiN circuitry and corresponding optical microscope picture. **b**, Architecture of the hybrid modulator after the integration of the $LiTaO_3$ and corresponding optical microscope picture. **c**, Architecture of the MZM after the fabrication of the electrodes and corresponding optical microscope picture. G, ground; S, signal. **d**, Overview of a 7-mm-long heterogeneous Si and SiN/$LiTaO_3$ MZM.

190 GBaud is successfully demonstrated, highlighting the potential of this approach for next-generation high-speed photonic applications.

Results

Design and fabrication of the $LiTaO_3$ modulator

The device architecture relies on an MZM implemented on a cutting-edge Si-PIC platform (imec iSiPP200). A subset of the commercial platform is used for device layout and circuit routing. Here only the silicon and silicon nitride waveguide layers are processed. The routing and splitting in the modulator is done in the silicon waveguide layer. The 50:50 splitter and combiner in the MZM are 1 × 2 multi-mode interferometers (MMIs), which are available in the PDK. Light is coupled in and out of the chip using grating couplers, and routing is performed by single-mode waveguides, which are included in the PDK. The schematic of the passive device architecture and an optical microscope picture of the fabricated circuit are depicted in Fig. 2a.

In a back-end of line heterogeneous integration step, X-cut thin-film $LiTaO_3$ is incorporated onto both arms of the MZI, hence enabling hybrid phase modulators. The integration of this EO material is achieved using µTP technology[27,36]. The µTP process allows for the transfer of thin films with a large length-to-width ratio. Here a commercial $LiTaO_3$-on-insulator (LTOI) wafer is used as the source for the transfer, on which suspended $LiTaO_3$ membranes are prepared. These measure 300 nm in thickness, 30 µm in width and 7 mm in length. Details on the fabrication process flow of the suspended membranes and the back-end integration are provided in Methods and in Extended Data Fig. 1.

These membranes are then transferred to the photonic chip using a commercial micro-transfer printer, after applying a 50-nm-thick layer of benzocyclobutene (BCB) on the chip as an adhesive. A schematic of the device and the corresponding optical microscope pictures after the successful integration of the $LiTaO_3$ on the platform are illustrated in Fig. 2b. Utilizing the versatility of the µTP approach, the modulator operates in a push–pull configuration, with the printed $LiTaO_3$ membranes oriented 180° relative to one another. This allows the use of integrated electronic drivers with a differential output[37]. The influence of µTP on the SiPho circuitry is investigated in Extended Data Fig. 5 and found to be negligible.

After integration, the final metallization step involves depositing a 20 nm layer of titanium (Ti) followed by a 1 µm layer of gold (Au) using a lift-off process. This step is required to form the metal electrodes configured in a ground–signal–signal–ground (GSSG) arrangement on top of the device arms. The schematic of the finalized MZM, along with a detailed optical microscope view, is shown in Fig. 2c. The entire modulator is depicted in Fig. 2d.

A critical feature of the device is the efficient coupling of light from the Si waveguide to the hybrid EO section of the MZM. This coupling is achieved through an adiabatic transition. In the design, both the Si and the SiN layers of the Si photonic platform are utilized to minimize the coupling loss into the EO structure. A schematic of the coupling structure, along with the optical mode profiles for each region of interest, is shown in Fig. 3. With the vertical tri-layer stack of Si/SiN/$LiTaO_3$, a transition is designed to be robust against fabrication geometry variations, for example, the layer thickness of SiN and $LiTaO_3$ or waveguide dimensions. The simulated transmission efficiency, depicted in Fig. 3b, is computed using the eigenmode expansion method implemented in the commercial software Ansys Lumerical MODE (2022 R2), for a range of taper lengths, and shows that a coupling efficiency of virtually 100% is possible in this hybrid structure. Further details on the adiabatic transition design are provided in Methods. Excluding the coupling section,

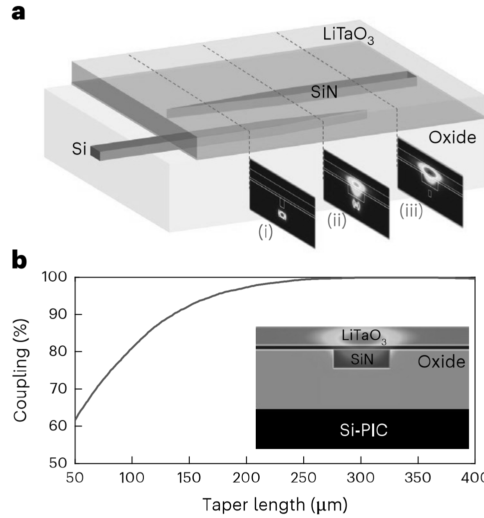

Fig. 3 | Transition from the Si waveguide to the hybrid modulator. a, Schematic of the tri-layer adiabatic transition: mode profiles in the regions of interest are added. **b**, Expected transmission from a Si waveguide to a hybrid SiN/$LiTaO_3$ phase modulator and (inset) cross-section of the passive stack of an MZM arm.

the effective length of the active EO SiN/$LiTaO_3$ waveguide is reduced to 6.6 mm, compared to the original 7 mm length of the modulator arms, since a 200 μm transition length was chosen.

Performances of the modulator

The fabricated MZMs are characterized both optically and electro-optically. Initial characterization involves a transmission wavelength sweep in the O band, spanning from 1,300 nm to 1,325 nm. Continuous-wave optical power is coupled to the chip using a tunable laser. Through an optical fibre and a polarization controller, the transverse electric mode is exited in the waveguide via a grating coupler. The optical power transmitted through the MZM is recorded using a power meter, while on the same structure set, a reference waveguide transmission sweep is conducted to account for the contributions of the grating couplers and Si routing.

The resulting normalized MZM transmission spectrum is plotted in Fig. 4a, where the interference pattern reveals a spectral interferometric pattern with a free spectral range of 4 nm and an extinction ratio of 28 dB at a wavelength of 1,310 nm. Similar results are illustrated in Extended Data Fig. 2 for all MZMs. However, beyond the 3.8 dB insertion loss of the MZM structure defined by the platform PDK, the high-speed EO modulation section introduces an additional 2.9 dB insertion loss, including coupling (0.6 dB) and propagation losses (0.7 dB). The remaining loss is attributed to a misalignment of around 0.6 μm of the final Au layer, which introduces an additional 1.6 dB of optical loss. Further details on the losses of the MZM are available in Extended Data Table 2.

Next, the device is operated in a quasi-DC modulation experiment. The transmitted continuous-wave optical signal is modulated at low electrical frequencies to characterize the half-wave voltage (V_π). The device is driven by a radio frequency (RF) triangular wave at 100 kHz, generated by an RF signal generator, while the optical wavelength of 1,309.26 nm is chosen to correspond to the quadrature operating point of the modulator, enabling operation in the linear modulation regime. The electrical signal is applied to the device using an RF probe, and the optical power transmitted through the device is recorded using a photodetector and an oscilloscope. This result is then plotted as a function of the applied voltage. The results, shown in Fig. 4b, reveal a V_π of 7.0 V for a single phase shifter (one arm of the MZM), which corresponds to 3.5 V in the push–pull amplitude modulation configuration (both arms of the MZM). This yields a voltage–length product ($V_\pi L$) of 2.3 V cm, consistent with recent reports on $LiTaO_3$ MZMs fabricated on the LTOI platform[21,23]. Moreover, when comparing this result to the expected V_π curve, calculated using finite element method simulations in combination with an analytical model, it demonstrates excellent agreement with the measurement as depicted in the overlay in Fig. 4b. More information on the simulation of V_π is available in Methods.

The high-speed response of the device is characterized in twofold: first, the electrodes are characterized by performing an electrical-to-electrical (EE) measurement, and afterwards, the full electrical-to-optical-to-electrical (EOE) response is measured. The EE responses are measured with a vector network analyser (VNA) connected to the chip with a set of GSSG probes, as shown in Fig. 5a. Here the electrical transmission of the transmission lines is characterized. This measurement is carried out on two different chips. On the first chip, the modulator is fabricated on a wafer with a regular Si substrate. In the second case, a high-resistivity (HR) Si substrate is used as the wafer substrate. The comparison between the two lines, presented in Fig. 5b, demonstrates a clear enhancement of the RF bandwidth when using the HR Si substrate owing to lower absorption loss of the RF wave in the substrate. The high-resistive silicon substrate with very few free carriers has a low loss tangent, and the silicon substrate RF losses become negligible. The losses in the RF transmission line are in this case mainly dominated by losses of the metal lines. By reducing these substrate losses, the bandwidth can be increased, mainly by avoiding the rapid increase of the substrate RF losses with frequency[38,39].

The EOE response of the MZMs, fabricated on a standard and an HR Si substrate, is then measured using a similar experimental set-up (Fig. 5c). The device is connected to one port of the VNA using a GS probe on one side, and the opposite side of the device is terminated with a 50 Ω load, to prevent electrical reflections at the far side. Continuous-wave optical power is coupled from the laser to the Si-PIC with an optical fibre, transmitted through the MZM, out-coupled and converted into an electrical signal by a high-speed photodetector. The resulting signal is received at the second port of the VNA. The EOE frequency response of the MZMs is presented in Fig. 5d for both modulator types. Again, the device with an HR substrate demonstrates a much higher 3 dB cut-off frequency in excess of 70 GHz, limited by the experimental set-up (the bandwidth of the VNA and the photodetector).

Data transmission

As a demonstration, the device is utilized in a link to transmit data for which the set-up is presented in Fig. 6a. A differential signal, generated by a 256 GS s^{-1} arbitrary waveform generator (AWG), is applied to the device using a GSSG probe. A second probe is used to terminate the

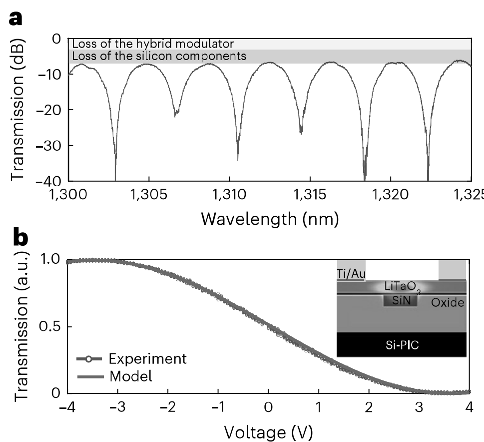

Fig. 4 | Quasi-DC characterization of the modulator. a, Measurement of the modulator transmission as a function of wavelength. **b**, Normalized transmission of the modulator as a function of applied voltage as well as the simulated response and (inset) cross-section of the full stack of an MZM arm.

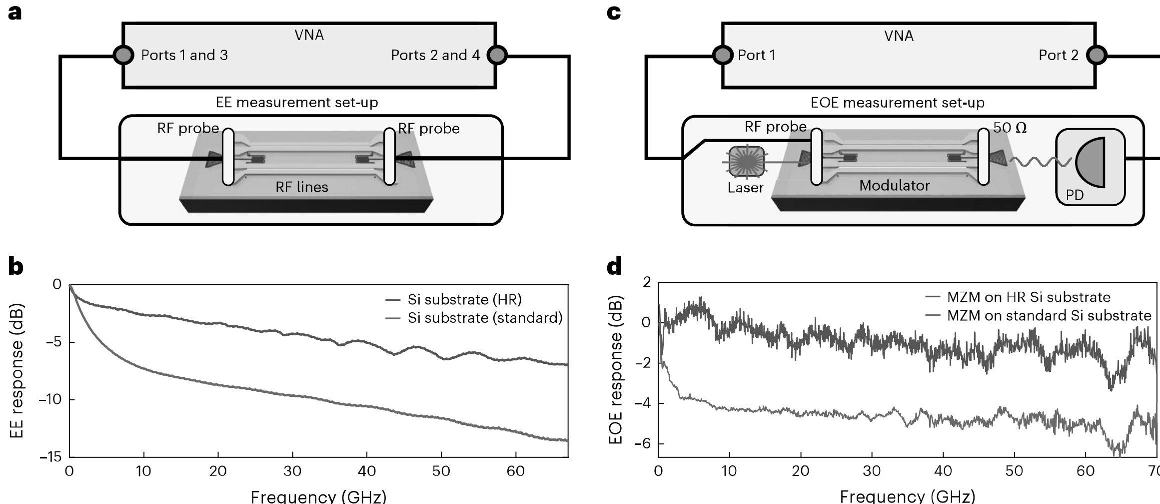

Fig. 5 | High-speed characterization of the modulator. a, EE measurement set-up for the RF line frequency response characterization. **b**, Results showing the comparison using regular Si substrate and HR substrate. **c**, EOE measurement set-up for the modulator frequency response characterization. **d**, Results showing the comparison for a modulator integrated on a platform using a regular Si substrate and HR substrate. PD, photodetector.

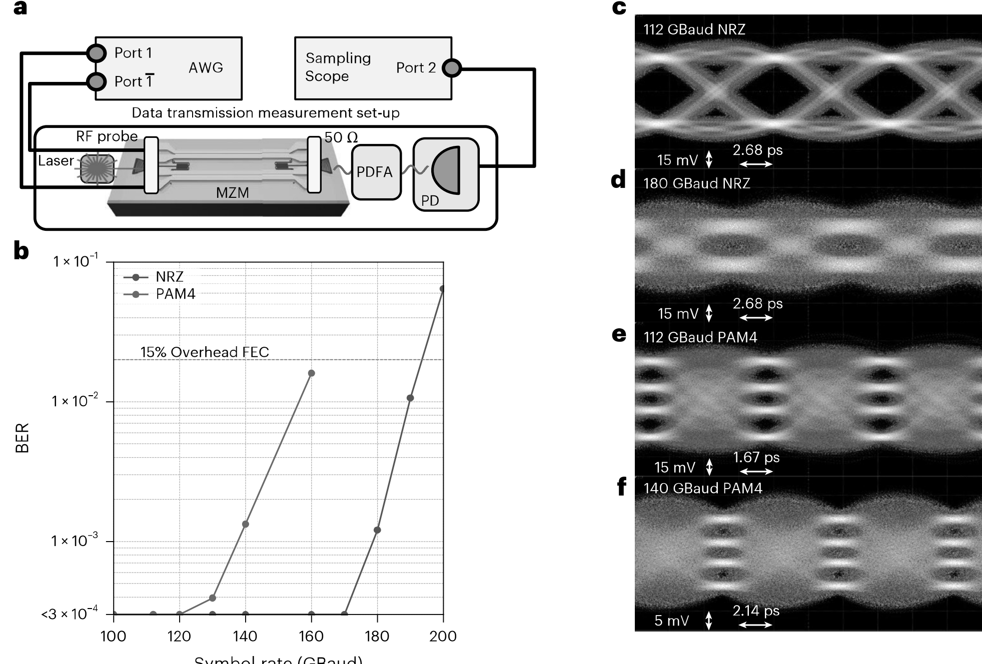

Fig. 6 | Data transmission experiment. a, Measurement set-up for eye-diagram measurements. **b**, BER in the transmitted bit sequence for NRZ (blue) and PAM4 (red) measured signals. A horizontal dashed line indicates the threshold for FEC with an overhead of 15%. **c**–**f**, Eye diagrams for 112 GBaud NRZ (**c**), 180 GBaud NRZ (**d**), 112 GBaud PAM4 (**e**) and 140 GBaud PAM4 (**f**); all figures used correction at the transmitter side and a 64-tap FFE on the receiver side; however, no offline digital post-processing was done.

device on the opposite side of the transmission line with two 50 Ω loads to prevent electrical reflections. The optical signal is amplified using a praseodymium-doped fibre amplifier (PDFA) before being detected by a high-speed photodetector. The detected signal is subsequently recorded using a sampling oscilloscope. To optimize the transmission, the link is characterized to facilitate the equalization of the signal generated by the AWG. As such, clear eye diagrams are generated. Extended Data Fig. 4 shows the measured frequency response of the data transmission link (magnitude in a and phase in b), which is compensated at the AWG. A noticeable performance drop-off is observed in the link characterization around 70 GHz, attributed to the bandwidth limitations of the electrical cables, RF probes, the high-speed photodetector and the AWG. All transmitted signals are based on standardized pseudorandom bit sequences (PRBS-15).

A 64-tap feed-forward equalization (FFE) algorithm is applied at the receiver end, using the sampling oscilloscope's software to enhance the received signal. Figure 6b presents the measured bit error rate (BER) derived from the generated eye diagrams using both non-return-to-zero (NRZ) and pulse-amplitude modulation 4-level (PAM4) formats. A dashed line indicates the BER threshold for a forward error correction (FEC) algorithm with an overhead of 15%. The lower limit of the plot, at 3×10^{-4}, indicates the error rate threshold

below which statistically significant assessments could not be made, owing to the limited number of bits transmitted during the demonstration. Figure 6 also includes representative eye diagrams, all of which incorporate FFE.

Discussion

Performance improvement

High-speed hybrid EO/Si-PIC modulators are designed for integration into data communication systems, encompassing both inter- and intra-data centre links to enable massive data transmission. In such systems, power consumption is a critical parameter. The presented devices demonstrate considerable potential for further optimization in this regard, particularly through the reduction of electrical driving power.

Recently, high-quality etching of $LiTaO_3$ has been demonstrated[21]. By using this etching process, the $LiTaO_3$ layer in the hybrid modulator can be patterned. The patterned $LiTaO_3$ layers would allow for better confinement and hence a stronger EO effect as the electrode separation can be reduced (Extended Data Fig. 3). Consequently, the gap can be reduced from 5.5 µm to 3.4 µm, resulting in a stronger RF field and a lower simulated V_π of 2.7 V, corresponding to a simulated voltage–length product of 1.8 V cm. As discussed in Methods, for this configuration, efficient adiabatic couplers can be made on the platform that allow for high coupling efficiency of more than 99%. Moreover, proper design allows similar very high coupling efficiencies (>99%) for transverse misalignments of the $LiTaO_3$ ridge waveguide of up to 0.5 µm. These misalignments remain within the alignment accuracy specifications of wafer-scale µTP tools.

Conclusion

The successful heterogeneous integration of lithium tantalate onto a SiPho platform with minimal insertion loss is demonstrated. Implemented on a standard 200 mm Si-PIC platform, our approach ensures seamless integration with existing platform PDK components while preserving their performance. By leveraging back-end integration, we maintain compatibility across the entire wafer stack, enabling efficient co-integration with critical components such as waveguides, heaters, filters and germanium photodetectors. The manufactured MZM achieves a measured bandwidth exceeding 70 GHz, limited by the measurement set-up, and exhibits a voltage–length product of 2.3 V cm comparable to the demonstrated LTOI platforms. The hybrid phase modulators in the MZM arms induce an additional 2.9 dB insertion loss. Lastly, high-speed transmission experiments are performed, reaching symbol rates of 190 GBaud (NRZ) and data rates of more than 320 Gbit s^{-1} (PAM4).

These results mark a notable step towards high-speed, high-performance hybrid lithium tantalate photonic platforms. They pave the way for scalable, industry-compatible EO integration for low-energy consumption data communication links that can be fabricated in high volumes.

Online content

Any methods, additional references, Nature Portfolio reporting summaries, source data, extended data, supplementary information, acknowledgements, peer review information; details of author contributions and competing interests; and statements of data and code availability are available at https://doi.org/10.1038/s41566-025-01832-9.

References

1. Sneh, A. & Doerr, C. R. in *Integrated Optical Circuits and Components* (CRC Press, 1999).
2. Zhou, X., Yi, D., Chan, D. W. U. & Tsang, H. K. Silicon photonics for high-speed communications and photonic signal processing. *npj Nanophoton.* **1**, 1–14 (2024).
3. Lischke, S. et al. Ultra-fast germanium photodiode with 3-dB bandwidth of 265 GHz. *Nat. Photon.* **15**, 925–931 (2021).
4. Gass, K. OIF adds a short-reach design to its 1600zr/ zr+ portfolio. *Gazettabyte* https://gazettabyte.com/oif-adds-a-short-reach-design-to-its-1600zr-zr-portfolio/ (2025).
5. Chelladurai, D. et al. Barium titanate and lithium niobate permittivity and Pockels coefficients from megahertz to sub-terahertz frequencies. *Nat. Materials* **24**, 868–875 (2025).
6. Wolf, S. et al. Silicon-organic hybrid (SOH) Mach-Zehnder modulators for 100 Gbit/s on-off keying. *Sci. Rep.* **8**, 2598 (2018).
7. Haffner, C. et al. All-plasmonic Mach–Zehnder modulator enabling optical high-speed communication at the microscale. *Nat. Photon.* **9**, 525–528 (2015).
8. Burla, M. et al. 500 GHz plasmonic Mach-Zehnder modulator enabling sub-THz microwave photonics. *APL Photon.* **4**, 056106 (2019).
9. Baeuerle, B. et al. 120 GBd plasmonic Mach-Zehnder modulator with a novel differential electrode design operated at a peak-to-peak drive voltage of 178 mV. *Opt. Express* **27**, 16823–16832 (2019).
10. Eppenberger, M. et al. Resonant plasmonic micro-racetrack modulators with high bandwidth and high temperature tolerance. *Nat. Photon.* **17**, 360–367 (2023).
11. Yamazaki, H. et al. IMDD transmission at net data rate of 333 Gb/s using over-100-GHz-bandwidth analog multiplexer and Mach-Zehnder modulator. *J. Light. Technol.* **37**, 1772–1778 (2019).
12. Estarán, J. M. et al. 140/180/204-Gbaud OOK transceiver for inter- and intra-data center connectivity. *J. Light. Technol.* **37**, 178–187 (2019).
13. Romagnoli, M. et al. Graphene-based integrated photonics for next-generation datacom and telecom. *Nat. Rev. Mater.* **3**, 392–414 (2018).
14. Liu, M. et al. A graphene-based broadband optical modulator. *Nature* **474**, 64–67 (2011).
15. Phare, C. T., Daniel Lee, Y.-H., Cardenas, J. & Lipson, M. Graphene electro-optic modulator with 30 GHz bandwidth. *Nat. Photon.* **9**, 511–514 (2015).
16. Wu, C. et al. Graphene-based silicon photonic electro-absorption modulators and phase modulators. *IEEE J. Sel. Top. Quantum Electron.* **30**, 1–11 (2024).
17. Wang, C. et al. Integrated lithium niobate electro-optic modulators operating at CMOS-compatible voltages. *Nature* **562**, 101–104 (2018).
18. Zhu, D. et al. Integrated photonics on thin-film lithium niobate. *Adv. Opt. Photon.* **13**, 242–352 (2021).
19. Wang, C. et al. Ultrabroadband thin-film lithium tantalate modulator for high-speed communications. *Optica* **11**, 1614–1620 (2024).
20. Wang, H. et al. Optical switch with an ultralow DC drift based on thin-film lithium tantalate. *Opt. Lett.* **49**, 5019–5022 (2024).
21. Wang, C. et al. Lithium tantalate photonic integrated circuits for volume manufacturing. *Nature* **629**, 784–790 (2024).
22. Zhang, J. et al. Ultrabroadband integrated electro-optic frequency comb in lithium tantalate. *Nature* **637**, 1096–1103 (2025).
23. Powell, K. et al. DC-stable electro-optic modulators using thin-film lithium tantalate. *Opt. Express* **32**, 44115–44122 (2024).
24. Yu, J. et al. Tunable and stable micro-ring resonator based on thin-film lithium tantalate. *APL Photon.* **9**, (2024).
25. Wandesleben, A. F. et al. Influences and diffusion effects of lithium contamination during the thermal oxidation process of silicon. *Adv. Eng. Mater.* **26**, 2400396 (2024).
26. X-Celeprint. Micro transfer printing is photonics heterogeneous integration made easy. www.x-celeprint.com (2025).

27. Roelkens, G. et al. Present and future of micro-transfer printing for heterogeneous photonic integrated circuits. *APL Photon.* **9**, 010901 (2024).
28. Churaev, M. et al. A heterogeneously integrated lithium niobate-on-silicon nitride photonic platform. *Nat. Commun.* **14**, 3499 (2023).
29. Ruan, Z. et al. High-performance electro-optic modulator on silicon nitride platform with heterogeneous integration of lithium niobate. *Laser Photon. Rev.* **17**, 2200327 (2023).
30. Chang, L. et al. Heterogeneous integration of lithium niobate and silicon nitride waveguides for wafer-scale photonic integrated circuits on silicon. *Opt. Lett.* **42**, 803–806 (2017).
31. Weigel, P. O. et al. Lightwave circuits in lithium niobate through hybrid waveguides with silicon photonics. *Sci. Rep.* **6**, 22301 (2016).
32. Vanackere, T. et al. Heterogeneous integration of a high-speed lithium niobate modulator on silicon nitride using micro-transfer printing. *APL Photon.* **8**, 086102 (2023).
33. Li, Z. et al. Photonic integration of lithium niobate micro-ring resonators onto silicon nitride waveguide chips by transfer-printing. *Opt. Mater. Express* **12**, 4375–4383 (2022).
34. Badri, S. H. et al. Compact modulators on silicon nitride waveguide platform via micro-transfer printing of thin-film lithium niobate. *Sci. Rep.* **15**, 11681 (2025).
35. Vandekerckhove, T. et al. High-efficiency second harmonic generation in heterogeneously-integrated periodically-poled lithium niobate on silicon nitride. In *The European Conference on Lasers and Electro-Optics* cd_3_2 (Optica Publishing Group, 2023).
36. Roelkens, G. et al. Micro-transfer printing for heterogeneous Si photonic integrated circuits. *IEEE J. Sel. Top. Quantum Electron.* **29**, 1–14 (2023).
37. Razavi, B. *Design of Analog CMOS Integrated Circuits* (McGraw-Hill, 2001).
38. Ponchak, G. Rf transmission lines on silicon substrates. In *European Microwave Conference* 1 (IEEE, 1999).
39. Witzens, J. High-speed silicon photonics modulators. *Proc. IEEE* **106**, 2158–2182 (2018).

Publisher's note Springer Nature remains neutral with regard to jurisdictional claims in published maps and institutional affiliations.

Springer Nature or its licensor (e.g. a society or other partner) holds exclusive rights to this article under a publishing agreement with the author(s) or other rightsholder(s); author self-archiving of the accepted manuscript version of this article is solely governed by the terms of such publishing agreement and applicable law.

© The Author(s), under exclusive licence to Springer Nature Limited 2026

Margot Niels [1,2,4] ✉, Tom Vanackere [1,2,4] ✉, Ewoud Vissers [1,2], Tingting Zhai [1,2], Patrick Nenezic [1,2], Jakob Declercq [2,3], Cédric Bruynsteen[2,3], Shengpu Niu[2,3], Arno Moerman [2,3], Olivier Caytan [2,3], Nishant Singh [2,3], Sam Lemey [2,3], Xin Yin [2,3], Sofie Janssen[2], Peter Verheyen[2], Neha Singh[2], Dieter Bode[2], Martin Davi[2], Filippo Ferraro[2], Philippe Absil[2], Sadhishkumar Balakrishnan[2], Joris Van Campenhout [2], Günther Roelkens [1,2], Bart Kuyken [1,2] ✉ & Maximilien Billet [1,2] ✉

[1]Department of Information Technology (INTEC), Photonics Research Group, Ghent University-imec, Ghent, Belgium. [2]imec, Leuven, Belgium. [3]Department of Information Technology (INTEC), IDLab, Ghent University-imec, Ghent, Belgium. [4]These authors contributed equally: Margot Niels, Tom Vanackere. ✉e-mail: Margot.Niels@UGent.be; Tom.Vanackere@UGent.be; Bart.Kuyken@UGent.be; Maximilien.Billet@UGent.be

https://doi.org/10.1038/s41566-025-01832-9

Methods

Process flow for heterogeneous $LiTaO_3$ integration

The fabrication of suspended $LiTaO_3$ membranes starts with a 300 nm $LiTaO_3$, on 2 μm oxide, on a Si substrate wafer (Extended Data Fig. 1a). The $LiTaO_3$ is patterned into rectangles of 30 μm × 7 mm with ultraviolet (UV) lithography, using an amorphous silicon (aSi) hard mask suitable for an argon-based reactive ion etching (RIE). The aSi hard mask is then removed in a potassium hydroxide solution (Extended Data Fig. 1b). As a second step, the oxide layer is patterned with UV lithography and RIE, after which the oxide is etched down to the Si substrate (Extended Data Fig. 1c). A mechanical encapsulation layer is then added, consisting of a photoresist layer exposed with UV lithography, which is subsequently developed. The patterns in the photoresist encapsulation are made in order to define mechanical links from the Si substrate to the $LiTaO_3$ membranes, allowing for the suspension of $LiTaO_3$ when the devices are released (Extended Data Fig. 1d). The last step is the releasing of the $LiTaO_3$ membranes in a wet etchant: buffered hydrofluoric acid (Extended Data Fig. 1e). The picture from Extended Data Fig. 1f shows an overview of the final sample. In this picture, 21 membranes of 30 μm × 7 mm are located on a sample of 2 mm × 7 mm. The membrane density is 1.5 membranes per mm^2, and for a 4-inch wafer, the total number of membranes would be more than 12,000.

At this step, the membranes are ready to be integrated on a different substrate. That substrate is prepared following the known practices of SiPho platforms. In this case, the Si and SiN device layers in the imec iSiPP200 platform are used. Starting from a silicon-on-insulator wafer with a 220 nm device layer, the Si layer is patterned with 2 etch depths (70 nm and 220 nm). Next, the wafer is planarized and a SiN layer with a thickness of 300 nm is deposited. This layer is patterned (with a full etch of 300 nm) and cladded in oxide, after which the wafer is planarized.

The prepared membranes are then picked using a polymer PDMS stamp, driven by a commercial micro-transfer printer tool (Extended Data Fig. 1g). For better adhesion, a BCB buffer layer is applied to the target before printing. The membranes are then placed on the host substrate, and the stamp is retracted, leaving the membrane at its final location (Extended Data Fig. 1h). The photoresist encapsulation is subsequently removed using an RIE oxygen plasma (Extended Data Fig. 1i), after which the BCB layer is cured at 280 °C for 90 min. An example of a Si chip with a cascade of 1-mm-long $LiTaO_3$ sections used as an insertion loss test structure is depicted in Extended Data Fig. 1j.

On top of the loss characterization test structures, the integration of $LiTaO_3$ membranes is done for four MZM devices. To illustrate the stability of the process flow, the transmission as a function of the wavelength of the devices is recorded and presented in Extended Data Fig. 2. The 4 devices, combining 8 $LiTaO_3$ integrated membranes in total, show similar results with an extinction ratio >25 dB for the peak near 1,310 nm. The wavelength sweeps in Extended Data Fig. 2 are normalized by subtracting the grating couplers and routing outside the actual MZM.

Loss characterization

Two kinds of optical loss contribution can be distinguished: propagation loss through the hybrid SiN/$LiTaO_3$ waveguide and the coupling or transition loss to get light from a Si waveguide to a hybrid SiN/$LiTaO_3$ waveguide (see adiabatic coupling for more details on this transition). To determine the propagation loss, hybrid SiN/$LiTaO_3$ waveguides with different lengths are fabricated. These are indicated as S1 and S2 in Extended Data Table 1 and have a propagation length of respectively 0.66 mm and 6.66 mm. For the transitions, two structures are prepared where one has only two transitions (one in, one out) and the other one has 28 transitions. Those are indicated as S3 and S4 in Extended Data Table 1 and have, in total, the same propagation length. Comparing the transmission of all structures and taking the propagation loss in the Si waveguides into account, a propagation loss of 1.0 ± 0.5 dB cm^{-1} and a transition loss of 0.3 ± 0.1 dB per transition can be deduced.

All component losses inside the MZM are also listed in Extended Data Table 2. The losses of the MMI splitter (C1) and Si routing (C2) are measured from the process control structures on the same chip. The transition from Si to SiN/$LiTaO_3$ (C3) and the propagation through the hybrid SiN/$LiTaO_3$ (C4) are extracted from the loss test structures as described above. Also, the introduction of metal traces on top of the $LiTaO_3$ (C5) introduces extra loss. A misalignment of about 600 nm is observed and can be seen in the focused ion beam cut. As no test structures are available to quantify this loss, a finite element method simulation was carried out in COMSOL to identify its contribution to be 1.6 dB.

Adiabatic coupling from Si platform to the hybrid $LiTaO_3$ modulator

An adiabatic tapering structure is optimized to efficiently couple the light from the Si waveguide to the EO section. This section describes the design for two versions of this coupling structure: the first is the taper section referred to when describing the fabricated chips (hybrid SiN/$LiTaO_3$-on-Si modulator), and the second is the version described in the discussion about performance improvement ($LiTaO_3$-on-Si modulator).

At the start of the first version of the transition, light remains confined within the Si waveguide despite the introduction of the $LiTaO_3$ layer, owing to the substantial refractive index contrast between the two materials as shown in Fig. 3a. At this stage, the relevant material stack consists of a 380 nm × 220 nm Si waveguide, encapsulated by a 500-nm-thick oxide layer and on top of that a 30 μm × 300 nm $LiTaO_3$ layer. Further in the transition structure, a 300 nm SiN layer is introduced, positioned 150 nm above the Si and 70 nm below the $LiTaO_3$ (Fig. 3a(i)). At this point, the SiN waveguide is tapered from a narrow tip (150 nm), ensuring that the optical mode remains predominantly in the Si, with minimal influence from that SiN taper tip. Subsequently, the SiN waveguide undergoes an adiabatic width expansion, after which the Si waveguide tapers down to 150 nm, facilitating a gradual transition of the optical mode from Si to the hybrid SiN/$LiTaO_3$ configuration (Fig. 3a(ii)). The SiN width is then adjusted to its final value of 900 nm to achieve the optimal confinement of the hybrid mode (Fig. 3a(iii)), determined as a trade-off between minimizing V_π by having as much as possible of the light in the $LiTaO_3$ layer and mitigating subsequent metal-induced losses by achieving sufficient confinement. In this configuration, the lateral alignment of the $LiTaO_3$ with the Si/SiN waveguides does not notably affect the efficiency of the transition. The taper dimensions are optimized using an eigenmode expansion solver in Lumerical, resulting in a final taper length of 200 μm. It should be noted that if the stack were cladded in oxide, this taper will have to be elongated in order to achieve the same performance.

As outlined in the main text discussion, the use of a patterned $LiTaO_3$ ridge waveguide enhances the modulator performance but requires an adjustment of the adiabatic transition geometry. In the first part of the transition, up until the hybrid $LiTaO_3$/SiN mode, the design is still similar (transition 1 in Extended Data Fig. 3a). Then, a second transition is added to the design (transition 2 in Extended Data Fig. 3a), where the mode is pushed from the hybrid SiN/$LiTaO_3$ (Extended Data Fig. 3a(i)) to a patterned $LiTaO_3$ configuration by introducing a 300 nm ridge waveguide on top of the slab (Extended Data Fig. 3a(ii)). The ridge waveguide starts with a taper tip of 150 nm and ends with a width of 1.35 μm after a width expansion over 50 μm. The last step of the transition is to taper down the SiN below (from 900 nm to 150 nm over 10 μm) to obtain a pure LTOI waveguide mode (Extended Data Fig. 3a(iii)). For this configuration, the design is sensitive to the lateral alignment of the SiN and $LiTaO_3$ waveguides. Nevertheless, with the typical alignment accuracy of the transfer printing technology of 500 nm 3σ, the coupling efficiency remains >99%, as seen in Extended Data Fig. 3b, making this configuration feasible using the process flow presented in this work.

Half-wave voltage calculation

As described before, both an MZM with hybrid SiN/$LiTaO_3$ EO sections and an MZM with LTOI ridge waveguide EO sections are considered in the V_π calculation. The simulations are done using a combination of multiple finite element method simulations in COMSOL and an analytical model. The EO phase shift ($\Delta\phi$) experienced by an MZM in a push–pull configuration is governed by the following expression:

$$\Delta\phi = \frac{2\pi n_e^4 \Gamma r_{33} V}{n_{\mathrm{eff}} \lambda G} L \quad (1)$$

where $n_e = 2.1269$ is the extraordinary refractive index, Γ represents the overlap factor between the RF and optical modes, $r_{33} = 30.5$ pm V^{-1} is the EO coefficient of $LiTaO_3$, V is the applied voltage, $L = 6.6$ mm is the effective length of one modulator arm, $\lambda = 1{,}310$ nm is the optical wavelength, n_{eff} is the effective refractive index of the optical mode and G denotes the electrode gap. The simulated parameters (Γ, n_{eff} and G) are listed in Extended Data Table 3.

From these simulations, the optimal electrode gap in the ridge configuration is smaller, which stems from the fact that the optical mode is more confined than in the hybrid waveguide, leading to the same optical loss from the metal (0.6 dB cm^{-1}). Using the equation and the simulation results, the theoretical values of V_π for an EO section with 6.6 mm length are calculated to be 3.6 V for the slab push–pull configuration and 2.7 V for the ridge push–pull configuration. The former value shows excellent agreement with measurements, whereas the latter configuration has not yet been fabricated and tested.

Impact of μTP on SiPho components

To evaluate the influence of μTP on SiPho devices, we focused on two representative components: a SiN ring resonator and a Si optical filter. Both structures were characterized before and after heterogeneous integration, including all μTP-related post-processing steps.

Before any processing, the ring resonator with a radius of 50 μm underwent a wavelength sweep around 1,310 nm, and a Q-factor of 104,005 was extracted. Following μTP and all associated post-processing steps, the same measurements were repeated, which revealed a Q-factor of 105,376. This variation remains within the bounds of measurement accuracy.

Furthermore, as illustrated in Extended Data Fig. 5, an optical filter (Extended Data Fig. 5a) was investigated, where light enters through the input port and propagates through a series of slightly detuned ring resonators. Each ring selectively couples a specific wavelength, enabling distinct spectral channels to emerge at the corresponding output ports. The wavelength sweeps on this filter show almost identical performance before (Extended Data Fig. 5b) and after (Extended Data Fig. 5c) μTP, including all the post-processing steps. These findings suggest that even more complex devices available within the SiPho platform are likely unaffected by the heterogeneous integration of $LiTaO_3$ via μTP.

Data availability

The datasets generated during and/or analysed during the current study are available from the corresponding authors on reasonable request.

Acknowledgements

We would like to acknowledge the contribution of imec's 200 mm pilot line for silicon photonics wafer fabrication and imec's PDK team for the mask tape-out. We also would like to acknowledge the contribution from P. Eswaran and S. Culhaoglu for the help in Si-PIC process development; S. Verstuyft, P. Geerinck, E. Özçeri and L. Van Landschoot for the help during the lithium tantalate device fabrication; and C. Krückel and J. Van Kerrebrouck for measurement support. Micro-transfer printing (μTP) is a technology under licence from X-Celeprint. We want to thank the European Space Agency for funding under the E/0365-70—NAVISP, LEO Project and the Research Foundation Flanders (FWO) for projects 3G035722 and 3F025420 and the FWO and F.R.S.-FNRS under the Excellence of Science (EOS) programme (40007560).

Author contributions

S.B., P.A., J.V.C., S.J., P.V., Neha Singh, D.B., M.D. and F.F. developed and fabricated the silicon nitride, silicon platform on 200 mm. M.N., T.Z. and M.B. fabricated the hybrid $LiTaO_3$/SiN devices and realized the heterogeneous integration. E.V., A.M., P.N. and O.C. performed the numerical simulations. E.V., A.M. and T.V. designed the devices. M.N. and T.V. performed the characterization (optical and quasi-DC). M.N., T.V., Nishant Singh, J.D., C.B. and S.N. performed the high-speed characterization and data communication experiment. M.N., T.V., B.K. and M.B. prepared the figures, data and the paper with input from other authors. P.A., S.L., X.Y., G.R., B.K. and M.B. supervised the project.

Competing interests

The authors declare no competing interests.

Additional information

Extended data is available for this paper at https://doi.org/10.1038/s41566-025-01832-9.

Correspondence and requests for materials should be addressed to Margot Niels, Tom Vanackere, Bart Kuyken or Maximilien Billet.

Peer review information *Nature Photonics* thanks the anonymous reviewers for their contribution to the peer review of this work.

Reprints and permissions information is available at www.nature.com/reprints.

https://doi.org/10.1038/s41566-025-01832-9

Extended Data Table 1 | Description and measured transmission for all test structures needed to determine the propagation loss and transition loss of the $LiTaO_3$ slabs

Amount of membranes (#)	Length of propagation in SiN/$LiTaO_3$ (mm)	Amount of transitions (#)	Si propagation loss (dB)	Transmission at 1310 nm (dB)
1	0.6	2	0.2 ± 0.01	− 8.2 ± 0.2
1	6.6	2	0.2 ± 0.01	− 8.8 ± 0.2
1	0.3	2	0.4 ± 0.01	− 8.1 ± 0.2
1	0.3	28	2.5 ± 0.04	−16.8 ± 0.2

https://doi.org/10.1038/s41566-025-01832-9

Extended Data Table 2 | Measurement of the loss for each component of the MZM, allowing to extract the contribution to the insertion loss from the Si-PIC PDK and the back-end integration process

Label	Component	Loss in the MZM
C1	MMI splitters	0.8 ± 0.2
C2	Si routing inside MZM	3.0 ± 0.4
C3	Transitions (Si to SiN/$LiTaO_3$)	0.6 ± 0.2
C4	EO section (SiN/$LiTaO_3$)	0.7 ± 0.3
C5	Metal misalignment	1.6 ± 0.1

Measurement of the loss for each component of the MZM, allowing to extract the contribution to the insertion loss from the Si-PIC PDK (C1 and C2) and the back-end integration process (C3, C4 and C5).

https://doi.org/10.1038/s41566-025-01832-9

Extended Data Table 3 | Parameters for a hybrid EO MZM and a ridge EO MZM configuration

Parameter	Hybrid EO waveguide	Ridge EO waveguide	Unit
Γ	0.454	0.393	–
n_{eff}	1.852	1.961	–
G	5.5	3.4	μm

 https://doi.org/10.1038/s41566-025-01832-9

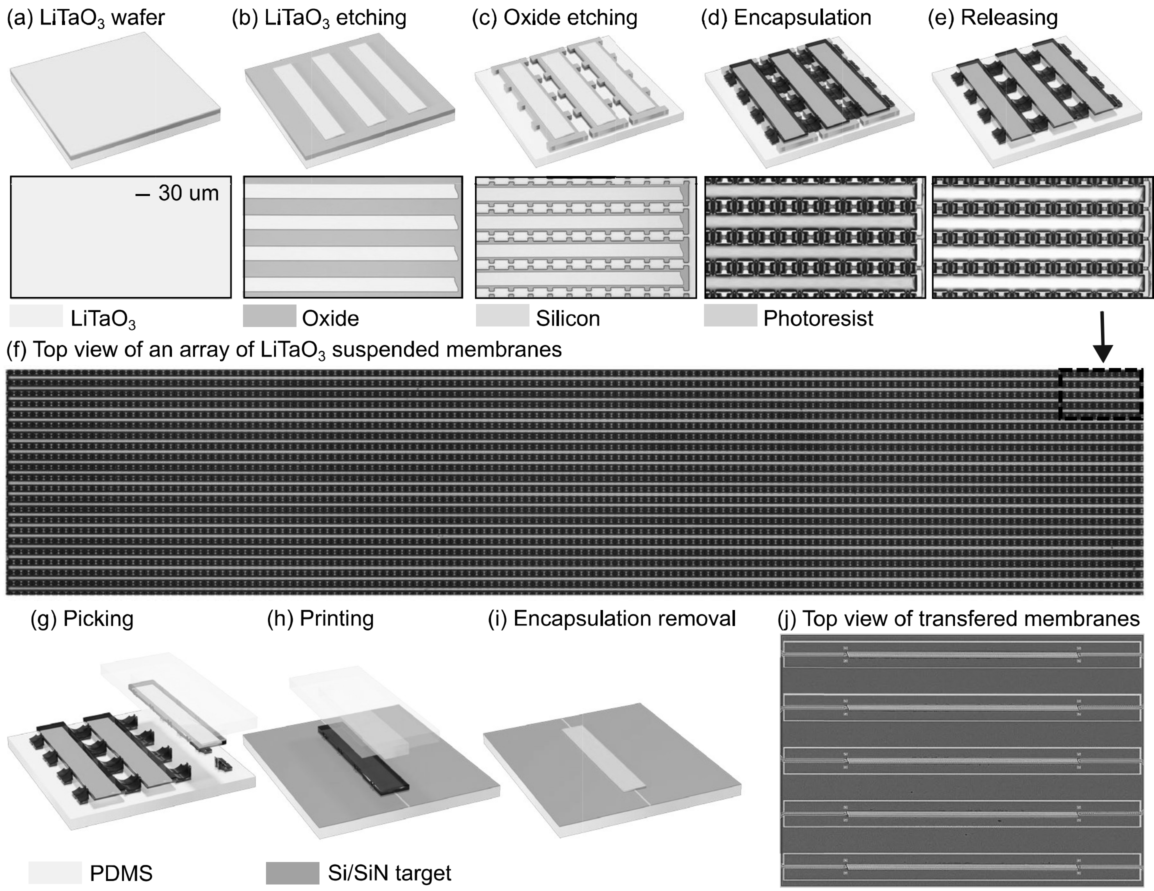

Extended Data Fig. 1 | Description of the successive steps for the fabrication and printing of suspended $LiTaO_3$ membranes with a schematic representation as well as a microscope picture. (**a**) $LiTaO_3$ (300 nm) / oxide (2 μm) / Si wafer (substrate) starting point. (**b**) Patterning of the $LiTaO_3$ membranes. (**c**) Patterning of the oxide release layer. (**d**) Photoresist mechanical encapsulation of the structures. (**e**) Undercutting (releasing) of the oxide layer, making the structures suspended. (**f**) Top view of the sample with suspended $LiTaO_3$. (**g**) picking of the suspended $LiTaO_3$. (**h**) Printing of the $LiTaO_3$ on a pre-processed external chip. (**i**) Encapsulation removal. (**j**) Top view of a few successfully printed $LiTaO_3$ membranes.

 https://doi.org/10.1038/s41566-025-01832-9

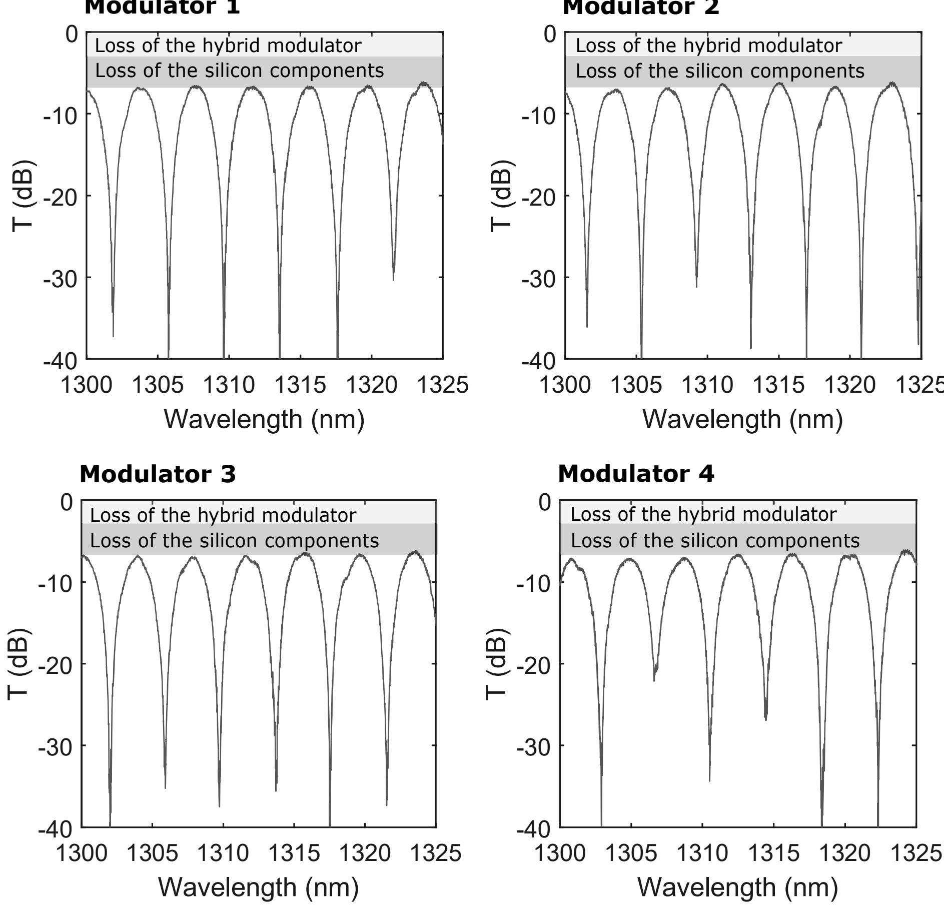

Extended Data Fig. 2 | Transmission measurements for four fabricated MZMs. Transmission (T) measurements for four fabricated MZMs. The losses from the grating couplers and external routing are removed. The insertion loss contribution from the Si-PIC components (C1 and C2 from Extended Data Table 2) and the contribution of the back-end integration process (C3, C4 and C5 from Extended Data Table 2) are described on top of the graphs.

https://doi.org/10.1038/s41566-025-01832-9

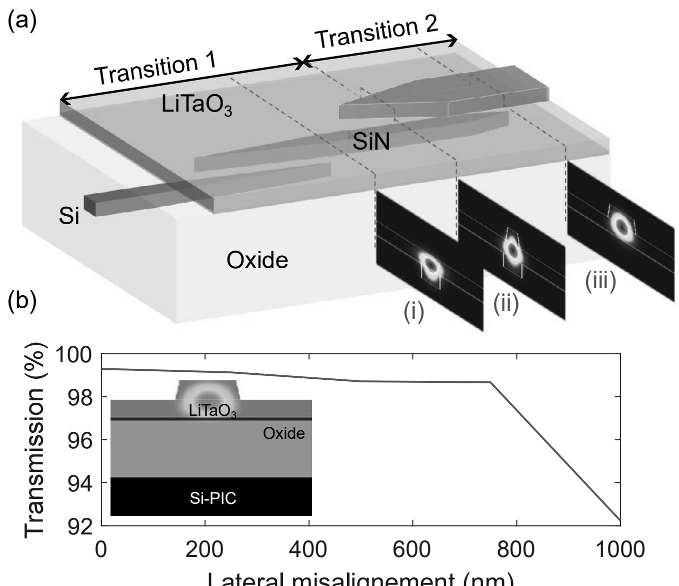

Extended Data Fig. 3 | Transition from the Si waveguide to a $LiTaO_3$ ridge waveguide. Transition from the Si waveguide to a $LiTaO_3$-on-insulator ridge waveguide. (**a**) Schematic of the tri-layer adiabatic transition. Mode profiles in the regions of interest are added. (**b**) Expected transmission from a Si waveguide to a ridge $LiTaO_3$ waveguide as a function of the lateral misalignment. (inset) Mode in the $LiTaO_3$-on-insulator waveguide.

https://doi.org/10.1038/s41566-025-01832-9

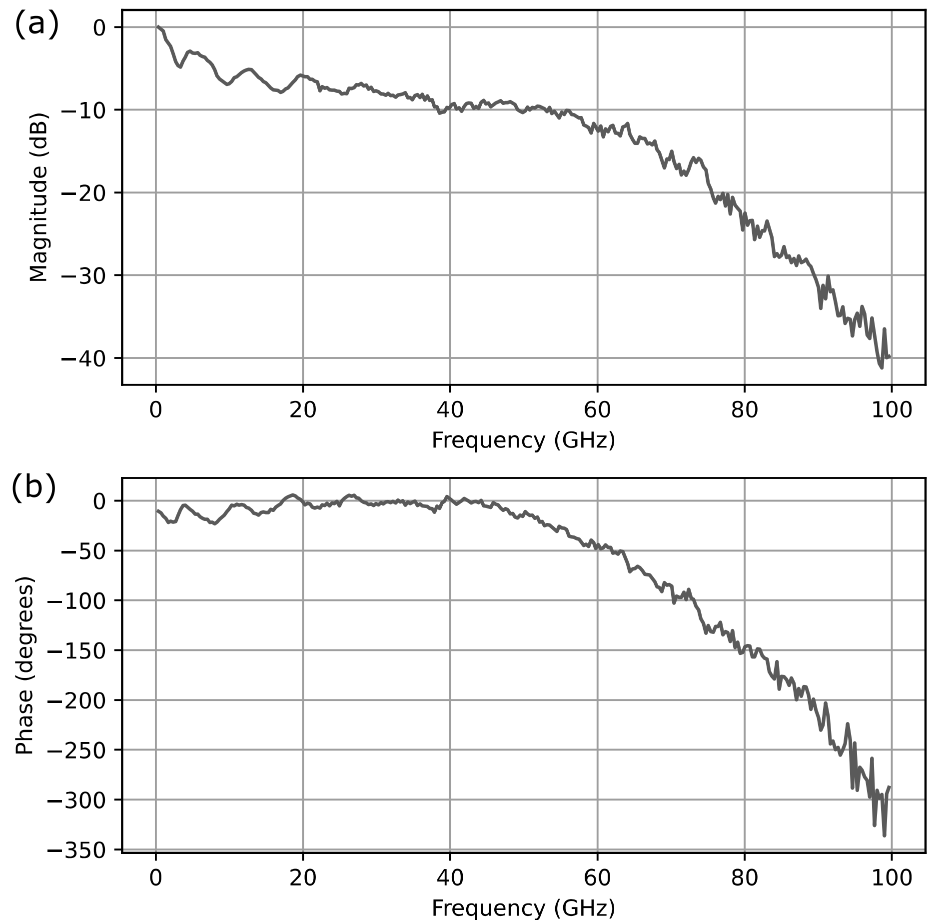

Extended Data Fig. 4 | Data transmission link characterisation. (**a**) Amplitude and (**b**) phase characteristic of the data transmission link, used to generate eye diagrams.

https://doi.org/10.1038/s41566-025-01832-9

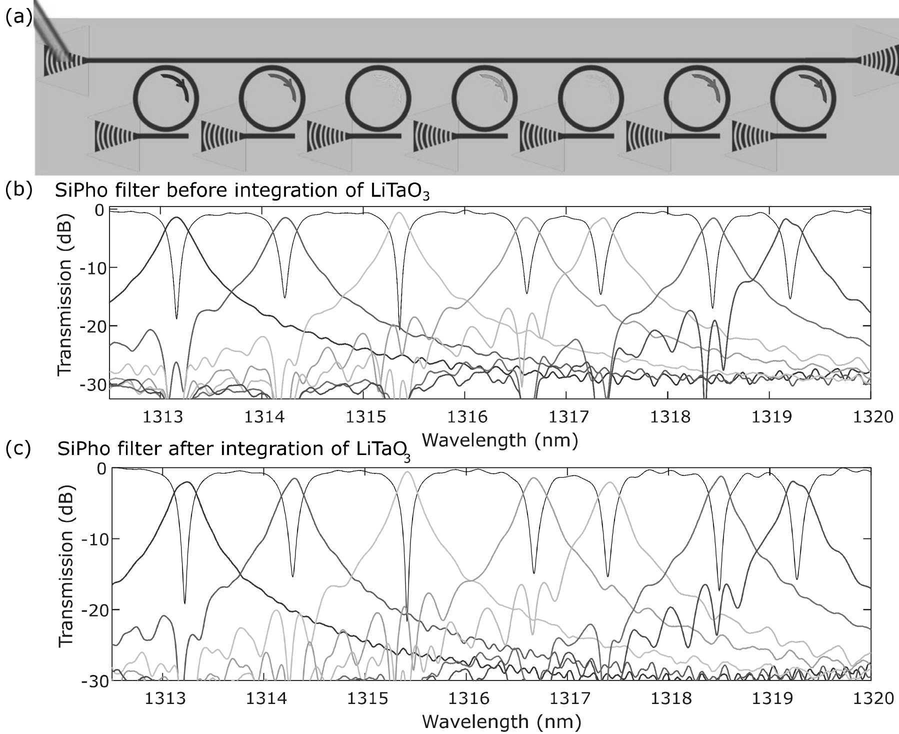

Extended Data Fig. 5 | Impact of micro-transfer printing on an optical filter. (**a**) Schematic representation of the optical filter (**b**) Spectrum before heterogeneous integration of $LiTaO_3$. (**c**) Spectrum after heterogeneous integration of $LiTaO_3$, showing very little influence of the micro-transfer printed $LiTaO_3$ membranes.